ACS OMEGA

http://pubs.acs.org/journal/acsodf

Article

Induced 2H-Phase Formation and Low Thermal Conductivity by Reactive Spark Plasma Sintering of 1T-Phase Pristine and Co-Doped MoS_2 Nanosheets

Cédric Bourgès, Ralph Rajamathi, C. Nethravathi,* Michael Rajamathi, and Takao Mori*

Cite This: *ACS Omega* 2021, 6, 32783−32790

Read Online

ACCESS | Metrics & More | Article Recommendations | Supporting Information

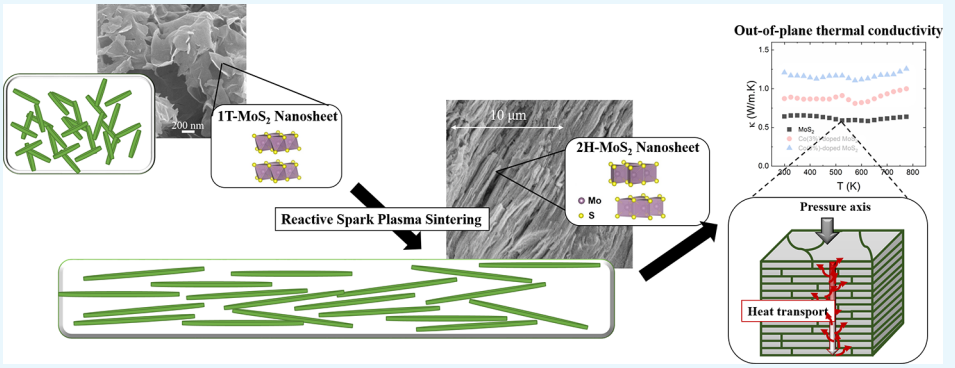

ABSTRACT: Pristine and Co-doped MoS_2 nanosheets, containing a dominant 1T phase, have been densified by spark plasma sintering (SPS) to produce a nanostructured arrangement. The structural analysis by X-ray powder diffraction revealed that the reactive sintering process transforms the 1T-MoS_2 nanosheets into their stable 2H form despite a significantly reduced sintering temperature and time testifying to the fast kinetics of phase change. Together with the phase conversion, the SPS process promoted a strong texturing of the nanosheets, which drives additional scattering processes and alters the electronic and thermal transport properties. In the pristine sample, it produced one of the lowest thermal conductivities ever reported on MoS_2 with a minimal value of 0.66 W/m·K at room temperature. The effect of Co substitution in the final sintered samples is not significant, compared to the pristine MoS_2 sample, except for a non-negligible improvement of the electrical conductivity by a factor of 100 in the high-Co content (6% by mass) sample.

1. INTRODUCTION

The layered transition-metal dichalcogenides (TMDC) are two-dimensional (2D) materials with the formula MX_2 (where M = group IVb, Vb, or VIb transition metal and X = S, Se, or Te). This material family has been intensively screened due to the substantial variety of transport (electronic and thermal) and structural properties.[1−4] Their layered structures are built as an assembly of two-dimensional covalently bonded X-M-X layers separated by a van der Waals gap leading to their crystallization in various polytypes such as 1T, 2H, 3R, 4H, and 6R phases (where the numeral quantifies the number of X-M-X layers per unit cell along the *c*-axis, while T, H, and R indicate trigonal, hexagonal, and rhombohedral symmetry, respectively).

Among this broad family of compounds, MoS_2 is considered as a versatile material due to its various physicochemical and structural properties as it changes from bulk to nanoscales.[5] Its major properties comprise high carrier mobility at room temperature and a layer-dependent bandgap varying from an indirect bandgap of 1.2 eV to a direct bandgap of 1.9 eV, which make it suitable for possible electronic and optoelectronic device applications. Its common polytypes are 2H-MoS_2 (space group: $P6_3/mmc$; $a \approx 3.16$ Å; $c \approx 12.30$ Å),[5] considered as the most stable form, the metastable 1T-MoS_2 (space group: $P\bar{3}m1$; $a \approx 3.19$ Å; $c \approx 5.95$ Å)[6] and its intermediate polymorphs 1T′, 1T″ 1T‴ and 3H-MoS_2 (space group: $R3m$; $a \approx 3.17$ Å; $c \approx 18.38$ Å).[5] Nowadays, the synthesis of a single/multi-layer MoS_2 is easy, which opens a large gateway for the development of new materials based on two-dimensional (2D) MoS_2. Indeed, 2D nanomaterials and thin films have recently drawn an increasing interest of the scientific community due to the technological development for realizing and using nanostructures in various fields such as sensor, catalysis, and

Received: August 25, 2021
Accepted: November 15, 2021
Published: November 23, 2021

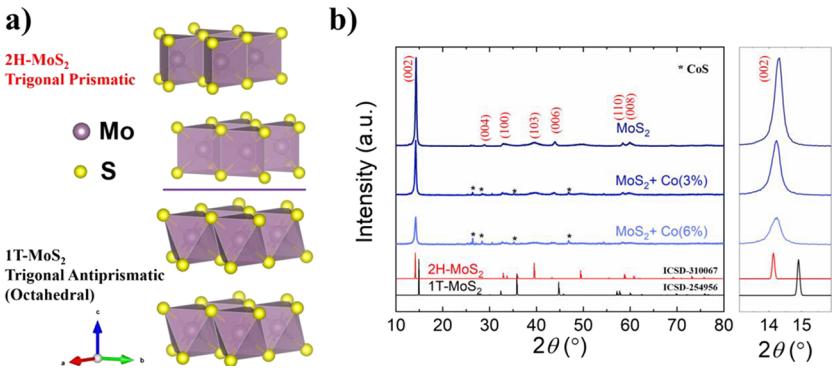

Figure 1. (a) Representation of the 1T and 2H crystal structure of MoS_2 and (b) X-ray powder diffraction patterns of MoS_2 samples after SPS.

thermoelectricity.[7−14] In the thermoelectric (TE) field, the material TE efficiency is quantified by the dimensionless figure of merit $zT = PF \times Tk^{-1} = S^2\sigma Tk^{-1}$ (PF, power factor; T, absolute temperature; S, Seebeck coefficient; σ, electrical conductivity; k, thermal conductivity). The nanostructuring approach presents a major interest due to the possibility to enhance the figure of merit zT by simultaneously reducing the thermal conductivity with selective phonon scattering effects and, possibly, increasing the Seebeck coefficient by the quantum confinement effect on carriers.[15−18] In particular, the thermal conductivity of layered materials have been of interest due to its anisotropic and interfacial effects.[19−25] The native bulk MoS_2 is reported to be an intrinsic p-type semiconductor with a large Seebeck coefficient ($S \approx 500-700$ μV/K@RT), but its poor electrical conductivity limits the overall power factor.[26,27] Combined with its relatively large thermal conductivity, the figure of merit zT is still reported to be negligible in comparison to other sulfide TE materials with values rarely exceeding $zT = 0.15$ even in the high-temperature range ($T \approx 1000$ K).[28] However, theoretical studies have estimated a high potential at room temperature of the MoS_2 nanoribbons with a predicted zT of about 3. This extraordinary value is obtained from mainly a high electrical conductivity induced by the reduction of the gap resulting in a strong edge reconstruction and gives an insight of the MoS_2's potential for TE applications by nanostructuring and/or enhancing electrical transport properties.[29] In a recent report, the calculated electronic structure revealed that a MoS_2 monolayer doped with Co becomes half-metallic due to the impurity band formation near the Fermi level. Considering the favorable substitution of Co in the Mo site by forming an S vacancy, it is also expected that the charge balance conservation will lead to hole doping, enabling the possibility to increase the carrier concentration of the MoS_2 and improve its electrical conductivity.[30,31] Moreover, the Co doping in MoS_2 has been reported, theoretically and experimentally, to induce dilute magnetism in the natively non-magnetic MoS_2.[30−32] Similar magnetism has also been reported to constructively promote a magnetic enhancement of the Seebeck coefficient, leading to a better TE performance.[33,34]

In a previous study, the development of Co-doped MoS_2 nanosheets composed of a dominant metastable 1T phase has been achieved with promising catalytic properties.[35] In the present study, we have investigated the densification of these 1T-MoS_2 nanosheets by reactive spark plasma sintering, which constitutes a nanostructure-engineering strategy for the development of the TMDC in contrast to the classical film approach usually employed.[36−39]

2. RESULTS AND DISCUSSION

2.1. Structural Characterization. The XRD pattern of the as-prepared undoped MoS_2 nanosheets before densification suggests that the sample is poorly ordered and exhibits increased basal spacing due to NH_3/NH_4^+ intercalation (Figure S1A). The as-prepared Co(6%)-doped MoS_2 nanosheets (Figure S1A) exhibits a broad (002) reflection at 11.0 Å, indicating the presence of a guest species in the interlayer. The guest entity could, possibly, be NH_3/NH^{4+} ions released as byproducts of hydrazine used as a reductant in the hydrothermal reaction. The asymmetric 2D reflections at $2\theta = 33$ and 57° reveal the presence of stacking faults within the few-layered Co-doped MoS_2. The SEM image (Figure S1B) of the as-synthesized Co(6%)-doped MoS_2 indicates that the sample consists of clusters of sheets.

Figure 1 displays the room temperature powder XRD patterns of the MoS_2 samples after reactive SPS sintering. The main diffraction peaks indicate that all the samples agree with the trigonal prismatic polymorph 2H−MoS_2 structure type (space group: $P6_3/mmc$; $a \approx 3.16$ Å; $c \approx 12.30$ Å) rather than the 1T−MoS_2 (Figure 1a) as highlighted by their respective simulated pattern in Figure 1b.[6] Interestingly, the dominant 1T phase of the initial powder of MoS_2 nanosheets (Supporting Information, Figure S1) has been fully converted into the 2H phase after a short SPS process (only 5 min of dwell time), indicating that the phase change kinetics between the trigonal antiprismatic and prismatic geometry is very fast.[35] Indeed, the 2H polytype is the thermodynamically stable form of TMDC-MoS_2 and it has been already reported that temperatures above 70−100 °C induces the 1T polytype to turn into 2H form, which is correlated experimentally with a strong endothermal signal.[5,40−42] A comparable signal has been confirmed in our current native nanopowder (Figure S2). The dynamical process of the transition between 1T/2H phases involves intra- and interlayer atomic plane gliding, which is caused by atom displacement due to extra thermal energy.[43] The 2H form has a hexagonal lattice with a threefold symmetry and an atomic stacking sequence (S−Mo−S′) of ABA. Each Mo atom in the 2H phase lies in a center prismatically coordinated by six surrounding S atoms, with the S atoms in the upper layer lying directly above those of the lower layer (Figure 1a). In contrast, the Mo atom in the 1T phase is octahedrally coordinated to six neighboring S atoms, with an atomic stacking sequence of ABC, where the bottom S′ plane occupies the hollow center of the top S lattice. For the 1T-to-2H transformation, the basic process involves a sulfur atomic plane gliding to hollow center sites due to thermal energy. The activation energy of this phase

https://doi.org/10.1021/acsomega.1c04646
ACS Omega 2021, 6, 32783−32790

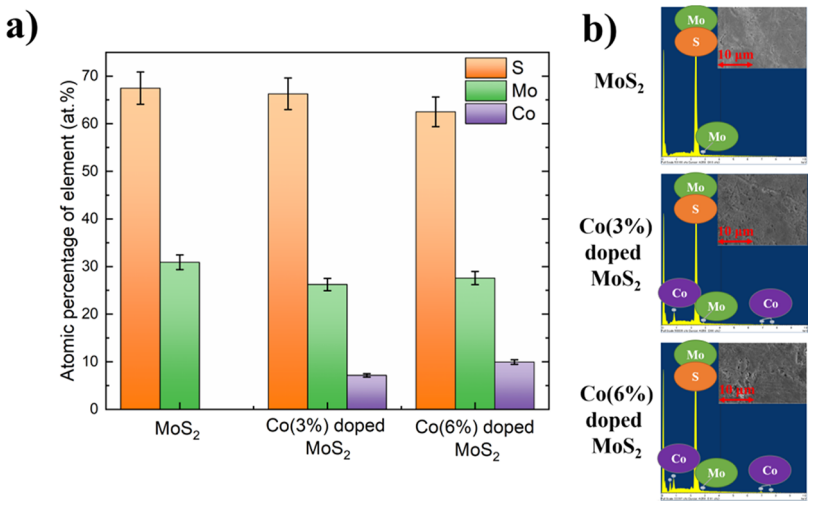

Figure 2. (a) Elemental analysis composition and (b) polished surface SEM image with the corresponding EDS spectrum of the MoS_2 samples after SPS.

transition mechanism is estimated to be 400 ± 60 meV (38 ± 6 kJ/mol).[44] The diffraction peaks corresponding to the (00*l*) indexation of the 2H-MoS_2 structure appear sharper and stronger than other peaks (as highlighted in Figure 1b), especially in the pristine sample, which are consistent with the preferential orientation due to the favorable ordering along the stacking direction. The other indexations ($hkl \neq 00l$) are characterized by a large full width at half maximum (FWHM), suggesting a reduced crystallite size or a possible strain in the structure. These observations have been confirmed and discussed later with the analysis by scanning electron microscopy (SEM) of a fractured cross section along the SPS pressure axis (Figure 3). With the increase in Co doping, the main diffraction peaks of the 2H-MoS_2 phase see their intensities significantly reduce and simultaneously, new diffraction peaks emerged from the background (* in Figure 1b). It clearly indicates that Co contained in the native nanosheets promotes the formation of byproduct phases during the reactive SPS step. This secondary phase seems to correspond to the CoS structure (space group: $P6_3/mmc$; $a \approx 3.37$ Å; $c \approx 5.17$ Å).[45] The formation of the secondary phase is consistent with the expected high reactivity of the raw powder composed of metastable nanosheets. Indeed, during the densification step, it has been confirmed that the sintering temperature has to be significantly reduced at 1223 and 1073 K for the pristine and the Co-doped samples, respectively, to reach the final consolidation step and to avoid the decomposition of the samples (Figure S3). However, below the sintering temperature, all the samples present sintering curves characteristic of a high reactivity process with an intermediate step (blue highlight in Figure S3). This intermediate step occurs below the pyrometer control, which makes it difficult to prevent the byproduct formation.

The energy-dispersive X-ray spectroscopy (EDS) elemental mapping (Figure 2 and Figures S4−S6) sustains the increasing amount of Co consistently with the expected doping level (Figure 2a) but reveals a disruption in the sample homogeneity in the Co-doped samples, attesting the by-product formation. The EDS point analysis indicates a representative composition close to CoS stoichiometry (Figure S7) in line with the XRD observation. Unfortunately, the limitation of the analysis accuracy did not allow us to obtain reliable composition values due to the fact that the characteristic energy peaks of Mo (Lα, 2.292 eV) and S (Kα, 2.309 eV) are too close and produced an uncertainty of the Mo/S quantification. Nevertheless, we can observe a (00*l*) peak shifting of the 2H-MoS_2 phase to the lower angle with the increasing content of Co, indicative of the *c* lattice expansion (Figure 1b). It suggests that the Co^{2+} dopant is still present in the MoS_2 lattice/interlayer. In previous studies, it has been demonstrated that Co^{2+} occupy the S vacancies in basal planes as well as the unsaturated S-edges produced by the hydrothermal synthesis of the MoS_2 nanosheets and confirmed experimentally by XPS analysis.[35,39,46,47] The Le Bail XRD refinement[48] of the (002) peak allows obtaining of a reasonable *c* parameter estimation of 2H-MoS_2 (space group: $P6_3/mmc$; $a \approx 3.16$ Å; $c \approx 12.30$ Å), which reveals that the average spacing between MoS_2 layers expands from 12.327(2) to 12.509(1) Å, respectively, for the pristine and the Co(6%)-doped MoS_2 samples. This is consistent with the increasing presence of Co in the interlayer planes of the MoS_2 phase. The EDS confirmed the increasing presence of Co in the MoS_2 matrix of the doped samples (Figure 2a) with the characteristic energy peaks (Lα, 0.776 eV and Kα, 6.924 eV) rising in the Co(3%)- and Co(6%)-doped samples compared to the pristine MoS_2 sample (Figure 2b).

The microstructure analysis by SEM imaging of the sample's cross section (Figure 3) confirms the oriented microstructure suggested by the XRD analysis. A strong texturing normal to the SPS pressure axis can be observed in the pristine sample (Figure 3a) and Co(3%)-doped sample (Figure 3b). In addition, it shows that the lateral dimensions of the sheets have significantly increased after SPS. The initial 1T nanosheets were a few-layer thick and a few hundred nanometers in the lateral dimension.[35] However, after SPS, the sheets have grown in the lateral dimensions into the micrometer range. It indicates that the initial nanosheets have, likely, merged for favoring the formation of a larger sheet along the in-plane axis. The anisotropic microstructure observed is consistent with the 2D-layered structure of 2H-MoS_2, wherein the weak van der Waals interaction between the layers will allow the layers to propitiously slide over one another due to the uniaxial pressure. The texturing is visibly reduced with the increasing Co content due to the formation of the secondary phase. Some inclusion of equiaxial grains, undoubtedly the secondary phase,

https://doi.org/10.1021/acsomega.1c04646
ACS Omega 2021, 6, 32783−32790

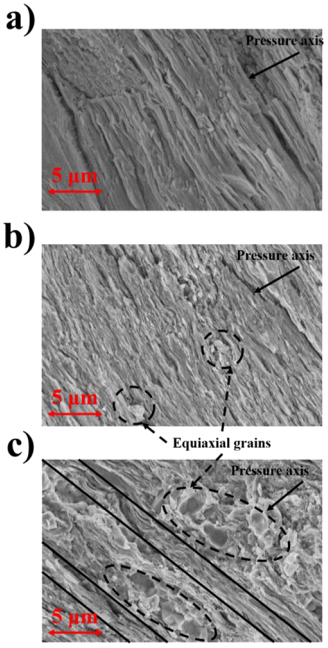

Figure 3. SEM micrograph of a fractured cross-sectional surface normal to the SPS pressure axis of (a) MoS_2, (b) Co(3%)-doped MoS_2, and (c) Co(6%)-doped MoS_2 samples after SPS.

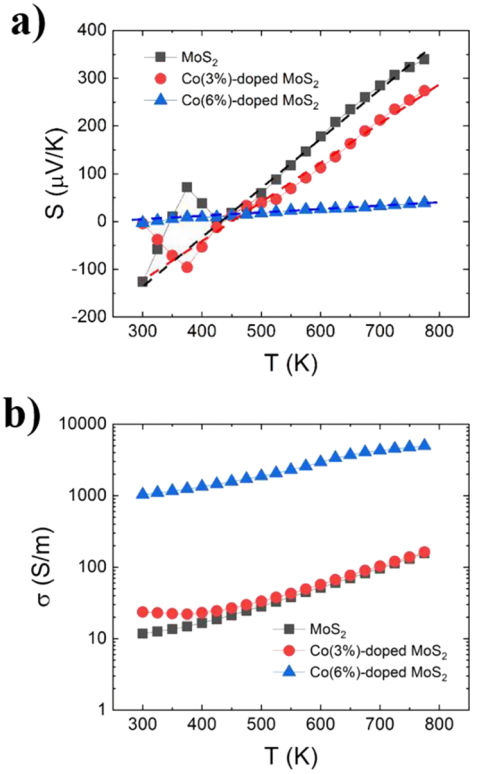

Figure 4. Temperature dependence of (a) Seebeck coefficient S and (b) electrical conductivity σ of the MoS_2, Co(3%)-doped MoS_2, and Co(6%)-doped MoS_2 samples after SPS.

appears in the Co-doped sample and becomes a non-negligible part of the microstructure in the Co(6%)-doped MoS_2 as displayed in Figure 3c. In this latter case, it seems that the MoS_2 layers are still present but, between layers, the equiaxial grains form a large agglomerate and break partially the global texturing.

2.2. Electrical Transport Properties. To observe the influence of the texturing and the phase change from 1T to 2H on the electrical properties, the temperature dependence of the in-plane electrical transport properties has been probed and the results are displayed in Figure 4. All the samples revealed a noticeable $n-p$-type transition behavior with the increasing temperature, indicated by the change of the sign of the Seebeck coefficient. This behavior seems to be in good agreement with the previous report on pristine bulk-MoS_2 composition.[28,49] At room temperature, all the samples exhibited a negative Seebeck coefficient (Figure 4a), indicating that electrons (n-type) are the major carriers and turn to positive values at higher temperatures (T > 500 K) indicative of the holes (p-type) dominating the transport properties. The band structure of the bulk 2H-MoS_2 is reported with an indirect bandgap of 1.29 eV and a Fermi level lying in the top of the valance band representative of the material's native p-type character.[50,51] To explain the observed n-type conduction at room temperature, we hypothesize that the reactive sintering process causes partial sulfur volatilization, leading to an excess of Mo remaining in the van der Waals gap as already reported in other TMDC.[52,53] Self-intercalated Mo will therefore provide additional electrons to the system, leading to an extrinsic n-type character at room temperature. Then, the $n-p$-type transition implies that the temperature rising activates hole carriers and turns the character to the native p-type semiconductor at a medium temperature in agreement with the intrinsic MoS_2 band structure. The chaotic trend, visible between 300 and 400 K in the pristine and Co(3%), is attributed to the expected competition between the native p-type behavior of the 2H-MoS_2 phase and the extrinsic n-type behavior produced by self-intercalation. The magnitude of the Seebeck coefficient is higher in the pristine sample, with values varying from $S = -126.14$@300 K to $S = +339.68$@775 K, compared to the Co-doped samples, with values from $S = -2.59$@300 K to $S = +39.02$@775 K for Co(6%)-doped MoS_2, for example. The variations of the Seebeck coefficient magnitude are associated with an apparent increase in the electrical conductivity in the Co-doped samples, especially for the larger content of 6% of Co (Figure 4b). According to the Mott equation prediction, the electrical conductivity increases with the carrier concentration and/or mobility and, reversely, the Seebeck coefficient decreases with the increase in carrier concentration.[54] It suggests that the current Co doping may increase the carrier concentration/mobility in our samples, which therefore can explain the drastic enhancement of the electrical conductivity together with the Seebeck coefficient decreasing. This experimental trend has been predicted by the electronic structure calculation performed on monolayer Co-doped MoS_2, showing the formation of impurity bands related to the Co substitution, which turns the behavior from the semiconductor to half-metallic.[31] In addition, so far, there is no report on CoS transport properties but some Co−S binary phases have been reported with n-type metallic transport properties.[55] It is, therefore, not excluded that the secondary phase affects the electrical transport properties by affecting the carrier concentration/mobility. To confirm the electrical behavior trend in a better way, Hall measurements were attempted to determine the charge carrier concentration in the pristine and doped samples. Unfortunately, the successive measurements remained unsuccessful or yielded inconsistent values attributed to several issues: the large sample resistance

https://doi.org/10.1021/acsomega.1c04646
ACS Omega 2021, 6, 32783−32790

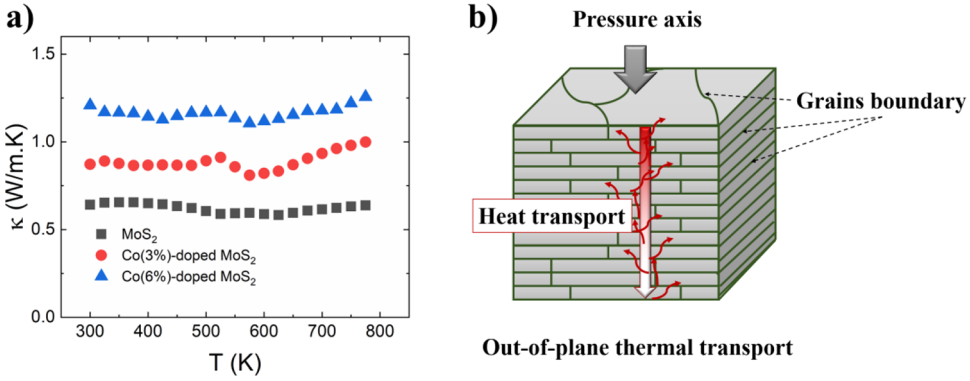

Figure 5. (a) Temperature dependence of the thermal conductivity of MoS_2, Co(3%)-doped MoS_2, and Co(6%)-doped MoS_2 after SPS and (b) schematic representation of the out-of-plane enhanced phonon scattering induced by the texturing.

Table 1. Representative Literature Comparison of the MoS_2 Thermal Conductivities

formatting	MoS_2 sample type	direction of measurement	κ (W/m·K)	temperature (K)	reference
single crystal	single crystal	basal	85−100	300	56
		c-axis	2−2.5	300	56
nanolayer	monolayer	basal	34.5	300	57
	multi-layer	basal	44−52	300	58
thin film	polycrystalline nanomembrane	in plane	0.75	300	38
	nanoflake film	in plane	1.5	300	60
	film with controlled grain orientation	out of plane	0.27−2	300	59
bulk (* correspond to the pristine MoS_2)	MoS_2 with $VMoS_4$ nanoinclusion	in plane	16−40*	300	28
		out of plane	4.2 - 6.7*	300	28
	MoS_2 with MoO_2 nanoinclusion	in plane	20−40*	327	49
		out of plane	3.1−5.5*	327	49
	exfoliated and restacked MoS_2	out of plane	1.05*	300	61
	this work	out of plane	0.71*−1.24	300	

(pristine sample), the presence of the secondary phase (Co-doped samples), and the *n*−*p*-type transition attesting to bipolar conduction near room temperature. All the samples show a positive temperature dependence of σ, agreeing with the semiconducting state of the phase. The pristine sample is characterized by a higher σ = 11.7 S/m@300 K compared to the literature value ($\sigma \approx$ 0.1−1 S/m@300−325 K) consistent with probable superior carrier mobility promoted by the texturing (Figure 3a). However, the absolute values remains too low for providing a large thermoelectric *PF* (Figure S8a). Despite the large σ enhancement, the *PF* of the Co(6%)-doped MoS_2 sample reduces significantly at high temperatures, compared to the pristine sample, due to the decrease in the Seebeck coefficient magnitude (Figure 4a). The maximum *PF* is obtained for the pristine sample with the highest values of 0.18 μW/cm·K^2@775 K.

2.3. Thermal Transport Properties. The measured out-of-plane thermal conductivity as a function of temperature is depicted in Figure 5a. The pristine sample exhibits an intrinsic low *k* varying between 0.66 and 0.71 W/m·K in the entire temperature range. These values are far lower than the native thermal conductivity of the MoS_2 single crystal (85−110 W/m·K in the basal plane)[56] and are one of the lowest ever reported for polycrystalline bulk samples (Table 1). Indeed, the thermal conductivity at room temperature of MoS_2 is reported to range from 34.5 W/m·K for monolayer MoS_2 to 52 W/m·K for 11-layer MoS_2.[57,58] Some recent papers report thermal conductivities below 1 W/m·K in polycrystalline thin films with a record lowest value of 0.27 W/m·K reported on polycrystalline films with perfect controlled grain orientation.[38,59,60] Experimentally, the out-of-plane thermal conductivity of bulk MoS_2 at 300 K is reported with values in a common range of 2.2−6.1 W/m·K and the lowest value of 1.05 W/m·K has been reported in restacked compounds with a similar 2H phase in the room temperature range.[28,49,61] This current state of the art ranks our samples in the lowest range of MoS_2 thermal conductivity ever reported. The significantly reduced thermal conductivity is consistent with the high texturization degree of the native nanosheets, which will consequently promote an enhanced phonon scattering. The increase in the phonon scattering is likely to be larger with the increased density of grain boundaries in the direction perpendicular to the pressure axis. The mean free path of phonon is then reduced due to the increase in the intergranular thermal resistance (Figure 5b). The rising grain boundary density, coupled with the possible presence of planar defects induced by the high kinetic conversion of the 1T phase into the 2H phase, like stacking faults, is possibly relevant additional contributors to the increase in phonon scattering.

The Co-doped samples are characterized by a slightly larger thermal conductivity than the pristine sample, which monotonously increases with the Co content. The origin of this phenomenon is likely governed by two interconnected contributions. First, the secondary phase formation (CoS) induced by the Co doping breaks the texturing of the sample and therefore induces a rise of the thermal transport along the out-of-plane axis (Figure 3c). Second, it is not excluded that this byproduct phase might be intrinsically characterized by a larger thermal conductivity than MoS_2.

https://doi.org/10.1021/acsomega.1c04646
ACS Omega 2021, 6, 32783−32790

Finally, the dimensionless figure of merit dependence on temperature, zT, has been quantified and revealed a direct dependency of the zT with the respective PF of each sample (Figure S8). Up to 600 K, the zT remains low in all series before rising up to the highest value of 0.02@775 K in the pristine sample.

3. CONCLUSIONS

We have achieved densification and texturing of 1T-MoS_2 nanosheets by reactive spark plasma sintering. This approach enables the possibility to significantly reduce the sintering temperature (<1000 °C) and time (∼5 min dwell time) as well as promoted a strong texturing of the MoS_2 nanosized layers as observed through XRD and SEM analysis. We highlight that the conversion of the metastable 1T to the stable 2H form is extremely fast and fully achieved by reactive densification. We report the lowest values of the out-of-plane thermal conductivity of the MoS_2 bulk material of 0.66−0.71 W/m·K in the pristine sample due to the nanosheet texturing. The Co-doped MoS_2 has been found to favor the formation of composite materials enhancing the electrical conductivity of the system by 100 times in the case of a large Co content. However, it induced a negative effect in the thermal conductivity and the magnitude of the Seebeck coefficient, which restricted the final zT.

4. EXPERIMENTAL SECTION

4.1. Preparation of Co-Doped MoS_2 Nanosheets. The cobalt-doped MoS_2 nanosheets were prepared as described previously.[35] An aqueous solution (45 mL) of a mixture of cobalt acetate (0.107 g) and ammonium tetrathiomolybdate (0.442 g) was stirred for 30 min. The second precursor acts as a source of ammonium, sulfur, and molybdenum in the reaction. At the end of 15 min, hydrazine hydrate (5 mL) was added to the solution and the stirring was continued. The black-brown solution was hydrothermally reacted in a Teflon-lined stainless-steel autoclave at 180 °C for 24 h and cooled to room temperature under ambient conditions. The black precipitate that formed was washed with distilled water till the pH of the washings was ∼7 followed by washing with acetone. The product was dried in air at ambient temperature. The preparation was repeated using 0.054 g of cobalt acetate to vary the cobalt content in the product. Cobalt contents were found to be ∼6 and 3% by mass in the samples prepared using 0.107 and 0.054 g of cobalt acetate, respectively,[35] and these samples would be called hereafter Co(6%)-doped MoS_2 and Co(3%)-doped MoS_2.

As a control experiment, the synthesis was repeated in the absence of cobalt acetate, which results in ammoniated MoS_2 nanosheets.

4.2. Densification by Spark Plasma Sintering. The ground powders were densified by spark plasma sintering (Dr. Sinter, SPS-322Lx) in a Ø10 mm graphite dye at various temperatures for 5 min of dwelling time under a uniaxial pressure of 50 MPa (heating and cooling rate of 100 K min^{-1}). The temperatures steps were 1223 and 1073 K, respectively, for the pristine MoS_2 and the two Co-doped MoS_2 samples (Figure S2). The densities measured by Archimedes' method were 4.52, 4.58, and 4.47, respectively, for the pristine, Co(3%)-, and Co(6%)-doped samples. It corresponds to ≥90% relative densities if normalized to the standard MoS_2 density. The sintered pellets were then cut and polished to the required shapes and dimensions for various measurements.

4.3. Characterization. The crystal structures of the sintered pellets were examined using X-ray powder diffraction (Rigaku Smart Lab 3 diffractometer) with Cu Kα radiation. Data were collected over a 2θ range of 10−120° with a step size of 0.02° and a step time of 2°/min. Le Bail fittings were performed using the FullProf program included in the WinPLOTR software.[48,62,63] The shape of the diffraction peaks was modeled using a pseudo-Voigt profile function. Zero-point shifts, asymmetry parameters, and lattice parameters were systematically refined, and the background contribution was manually estimated. Observations of microstructural aspects of the sintered samples were performed on the fractured cross section and polished surface using a Hitachi SU-4800 scanning electron microscope (SEM) and a mini-SEM (TM3000, Hitachi) both equipped with an energy-dispersive spectrometer (EDS).

The thermal diffusivity α and heat capacity C_p were measured using LFA-467 Hyperflash (Netzsch) under a flowing argon atmosphere (50 mL/min). The thermal conductivity κ was derived as a product of the sample's density (measured by Archimedes' method), thermal diffusivity, and heat capacity C_p. The measurements of electrical resistivity ρ and Seebeck coefficient S were performed simultaneously using a commercial instrument Ulvac ZEM-2 under partial helium pressure.

■ ASSOCIATED CONTENT

Supporting Information

The Supporting Information is available free of charge at https://pubs.acs.org/doi/10.1021/acsomega.1c04646.

Additional experimental details related to the structural, microstructural, and physico-chemical characterizations of the materials before and after densification (PDF)

■ AUTHOR INFORMATION

Corresponding Authors

C. Nethravathi − *Materials Research Group, Department of Chemistry, St. Joseph's College, Bangalore 560027, India; Department of Chemistry, Mount Carmel College, Bangalore 560052, India;* orcid.org/0000-0002-5000-7417; Email: nethravathic@gmail.com

Takao Mori − *WPI International Center for Materials Nanoarchitechtonics (WPI-MANA), National Institute for Materials Science (NIMS), Tsukuba 305-0044, Japan; Graduate School of Pure and Applied Sciences, University of Tsukuba, Tsukuba 305-8577, Japan;* orcid.org/0000-0003-2682-1846; Email: Mori.Takao@nims.go.jp

Authors

Cédric Bourgès − *WPI International Center for Materials Nanoarchitechtonics (WPI-MANA), National Institute for Materials Science (NIMS), Tsukuba 305-0044, Japan*

Ralph Rajamathi − *Materials Research Group, Department of Chemistry, St. Joseph's College, Bangalore 560027, India*

Michael Rajamathi − *Materials Research Group, Department of Chemistry, St. Joseph's College, Bangalore 560027, India;* orcid.org/0000-0002-4975-1855

Complete contact information is available at: https://pubs.acs.org/10.1021/acsomega.1c04646

https://doi.org/10.1021/acsomega.1c04646
ACS Omega 2021, 6, 32783−32790

Notes

The authors declare no competing financial interest.

■ ACKNOWLEDGMENTS

We acknowledge support from JST Mirai Program grant nos. JPMJMI19A1, JSPS KAKENHI JP19H00833, JP17H03749, and JP16H06441 and SERB, India grant no. EMR/2015/001982. The authors would like to thank Namiki Foundry (NIMS, Japan) for the use of the SEM facilities.

■ REFERENCES

(1) Manzeli, S.; Ovchinnikov, D.; Pasquier, D.; Yazyev, O. V.; Kis, A. 2D Transition Metal Dichalcogenides. *Nat. Rev. Mater.* **2017**, *2*, 17033.

(2) Hébert, S.; Kobayashi, W.; Muguerra, H.; Bréard, Y.; Raghavendra, N.; Gascoin, F.; Guilmeau, E.; Maignan, A. From Oxides to Selenides and Sulfides: The Richness of the CdI_2 Type Crystallographic Structure for Thermoelectric Properties. *Phys. Status Solidi A.* **2013**, *210*, 69−81.

(3) Zhou, C.; Zhu, H.; Pan, S.; Zheng, T.; Huang, X.; Lin, Q.; Yang, W. Determination of Band Alignments at 2D Tungsten Disulfide/High-k Dielectric Oxides Interfaces by x-Ray Photoelectron Spectroscopy. *Appl. Surf. Sci.* **2020**, *505*, 144521.

(4) Chowdhury, S.; Roy, A.; Liu, C.; Alam, M. H.; Ghosh, R.; Chou, H.; Akinwande, D.; Banerjee, S. K. Two-Step Growth of Uniform Monolayer MoS_2 Nanosheets by Metal-Organic Chemical Vapor Deposition. *ACS Omega* **2021**, *6*, 10343−10351.

(5) Gupta, D.; Chauhan, V.; Kumar, R. A Comprehensive Review on Synthesis and Applications of Molybdenum Disulfide (MoS_2) Material : Past and Recent Developments. *Inorg. Chem. Commun.* **2020**, *121*, 108200.

(6) Fang, Y.; Pan, J.; He, J.; Luo, R.; Wang, D.; Che, X.; Bu, K.; Zhao, W.; Liu, P.; Mu, G.; Zhang, H.; Lin, T.; Huang, F. Structure Re-Determination and Superconductivity Observation of Bulk 1T MoS_2. *Angew. Chem., Int. Ed.* **2018**, *57*, 1232−1235.

(7) Khan, K.; Tareen, A. K.; Aslam, M.; Wang, R.; Zhang, Y.; Mahmood, A.; Ouyang, Z.; Zhang, H.; Guo, Z. Recent Developments in Emerging Two-Dimensional Materials and Their Applications. *J. Mater. Chem. C* **2020**, *8*, 387−440.

(8) Li, D.; Gong, Y.; Chen, Y.; Lin, J.; Khan, Q.; Zhang, Y.; Li, Y.; Zhang, H.; Xie, H. Recent Progress of Two-Dimensional Thermoelectric Materials. *Nano-Micro Lett.* **2020**, *12*, 36.

(9) Mori, T.; Priya, S. Materials for Energy Harvesting: At the Forefront of a New Wave. *MRS Bull.* **2018**, *43*, 176−180.

(10) Petsagkourakis, I.; Tybrandt, K.; Crispin, X.; Ohkubo, I.; Satoh, N.; Mori, T. Thermoelectric Materials and Applications for Energy Harvesting Power Generation. *Sci. Technol. Adv. Mater.* **2018**, *19*, 836−862.

(11) Gooth, J.; Schierning, G.; Felser, C.; Nielsch, K. Quantum Materials for Thermoelectricity. *MRS Bull.* **2018**, *43*, 187−192.

(12) Nandihalli, N.; Liu, C. J.; Mori, T. Polymer Based Thermoelectric Nanocomposite Materials and Devices: Fabrication and Characteristics. *Nano Energy* **2020**, *78*, 105186.

(13) Joseph, D.; Navaneethan, M.; Abinaya, R.; Harish, S.; Archana, J.; Ponnusamy, S.; Hara, K.; Hayakawa, Y. Thermoelectric Performance of Cu-Doped MoS_2 Layered Nanosheets for Low Grade Waste Heat Recovery. *Appl. Surf. Sci.* **2020**, *505*, 144066.

(14) Kim, S.; Lee, C.; Lim, Y. S.; Shim, J. H. Investigation for Thermoelectric Properties of the MoS_2 Monolayer-Graphene Heterostructure: Density Functional Theory Calculations and Electrical Transport Measurements. *ACS Omega* **2021**, *6*, 278−283.

(15) Hicks, L. D.; Dresselhaus, M. S. Effect of Quantum-Well Structures on the Thermoelectric Figure of Merit. *Phys. Rev. B* **1989**, *37*, 12727−11107.

(16) Mori, T. Novel Principles and Nanostructuring Methods for Enhanced Thermoelectrics. *Small* **2017**, *13*, 1702013.

(17) Mao, J.; Liu, Z.; Ren, Z. Size Effect in Thermoelectric Materials. *npj Quantum Mater.* **2016**, *1*, 16028.

(18) Nethravathi, C.; Rajamathi, C. R.; Rajamathi, M.; Maki, R.; Mori, T.; Golberg, D.; Bando, Y. Synthesis and Thermoelectric Behaviour of Copper Telluride Nanosheets. *J. Mater. Chem. A* **2014**, *2*, 985−990.

(19) Wang, X. J.; Mori, T.; Kuzmych-Ianchuk, I.; Michiue, Y.; Yubuta, K.; Shishido, T.; Grin, Y.; Okada, S.; Cahill, D. G. Thermal Conductivity of Layered Borides : The Effect of Building Defects on the Thermal Conductivity of $TmAlB_4$ and the Anisotropic Thermal Conductivity of AlB_2. *APL Mater.* **2014**, *2*, No. 046113.

(20) McKinney, R.; Gorai, P.; Toberer, E. S.; Stevanovìc, V. Rapid Prediction of Anisotropic Lattice Thermal Conductivity: Application to Layered Materials. *Chem. Mater.* **2019**, *31*, 2048−2057.

(21) Kakefuda, Y.; Yubuta, K.; Shishido, T.; Yoshikawa, A.; Okada, S.; Ogino, H.; Kawamoto, N.; Baba, T.; Mori, T. Thermal Conductivity of $PrRh_{4.8}B_2$, a Layered Boride Compound. *APL Mater.* **2017**, *5*, 126103.

(22) Zhang, W.; Sato, N.; Tobita, K.; Kimura, K.; Mori, T. Unusual Lattice Dynamics and Anisotropic Thermal Conductivity in In_2Te_5 Due to a Layered Structure and Planar-Coordinated Te-Chains. *Chem. Mater.* **2020**, *32*, 5335−5342.

(23) Yu, X.; Shao, H.; Wang, X.; Zhu, Y.; Fang, D.; Hong, J. Anomalous Lattice Thermal Conductivity in Layered MNCl (M = Zr, Hf) Materials Driven by Lanthanide Contraction. *J. Mater. Chem. A* **2020**, *8*, 3128−3134.

(24) Grasso, S.; Tsujii, N.; Jiang, Q.; Khaliq, J.; Maruyama, S.; Miranda, M.; Simpson, K.; Mori, T.; Reece, M. J. Ultra Low Thermal Conductivity of Disordered Layered *p*-Type Bismuth Telluride. *J. Mater. Chem. C* **2013**, *1*, 2362−2367.

(25) Kaźmierczak-Bałata, A.; Grządziel, L.; Guziewicz, M.; Venkatachalapathy, V.; Kuznetsov, A.; Krzywiecki, M. Correlations of Thermal Properties with Grain Structure, Morphology, and Defect Balance in Nanoscale Polycrystalline ZnO Films. *Appl. Surf. Sci.* **2021**, *546*, 149095.

(26) Mansfield, R.; Salam, S. A. Electrical Properties of Molybdenite. *Proc. Phys. Soc., B* **1953**, *66*, 377−385.

(27) Thakurta, S. R. G.; Dutta, A. K. Electrical Conductivity, Thermoelectric Power and Hall Effect in *p*-Type Molybdenite (MoS_2) Crystal. *J. Phys. Chem. Solids* **1983**, *44*, 407−416.

(28) Kong, S.; Wu, T.; Zhuang, W.; Jiang, P.; Bao, X. Realizing *p*-Type MoS_2 with Enhanced Thermoelectric Performance by Embedding VMo_2S_4 Nanoinclusions. *J. Phys. Chem. B* **2018**, *122*, 713−720.

(29) Fan, D. D.; Liu, H. J.; Cheng, L.; Jiang, P. H.; Shi, J.; Tang, X. F. MoS_2 Nanoribbons as Promising Thermoelectric Materials. *Appl. Phys. Lett.* **2014**, *105*, 133113.

(30) Lin, X.; Ni, J. Charge and Magnetic States of Mn-, Fe-, and Co-Doped Monolayer MoS_2. *J. Appl. Phys.* **2014**, *116*, No. 044311.

(31) Wang, Y.; Li, S.; Yi, J. Electronic and Magnetic Properties of Co Doped MoS_2 Monolayer. *Sci. Rep.* **2016**, *6*, 24153.

(32) Martinez, L. M.; Delgado, J. A.; Saiz, C. L.; Cosio, A.; Wu, Y.; Villagrán, D.; Gandha, K.; Karthik, C.; Nlebedim, I. C.; Singamaneni, S. R. Magnetic and Electrocatalytic Properties of Transition Metal Doped MoS_2 Nanocrystals. *J. Appl. Phys.* **2018**, *124*, 153903.

(33) Vaney, J. B.; Aminorroaya Yamini, S.; Takaki, H.; Kobayashi, K.; Kobayashi, N.; Mori, T. Magnetism-Mediated Thermoelectric Performance of the Cr-Doped Bismuth Telluride Tetradymite. *Mater. Today Phys.* **2019**, *9*, 100090.

(34) Hébert, S.; Daou, R.; Maignan, A.; Das, S.; Banerjee, A.; Klein, Y.; Bourgès, C.; Tsujii, N.; Mori, T. Thermoelectric Materials Taking Advantage of Spin Entropy: Lessons from Chalcogenides and Oxides. *Sci. Technol. Adv. Mater.* **2021**, *22*, 583−596.

(35) Nethravathi, C.; Prabhu, J.; Lakshmipriya, S.; Rajamathi, M. Magnetic Co-Doped MoS_2 Nanosheets for Efficient Catalysis of Nitroarene Reduction. *ACS Omega* **2017**, *2*, 5891−5897.

(36) Imtiaz, M.; Chen, Z.; Zhu, C.; Naz, R.; Zada, I.; Pan, H.; Wang, D.; Abbas, W.; Nigar, S.; Li, Y.; Zhu, S. Three-Dimensional Aerogel Based on in-Situ Growth of 1T-MoS_2 on Functionalized Hierarchical Porous Carbon/Reduced Graphene Oxide for Energy Storage. *Appl. Surf. Sci.* **2020**, *506*, 144811.

https://doi.org/10.1021/acsomega.1c04646
ACS Omega 2021, 6, 32783−32790

(37) An, S.-J.; Park, D. Y.; Lee, C.; Bang, S.; Nguyen, D. A.; Kim, S. H.; Kim, H. Y.; Jeong, H. J.; Jeong, M. S. Facile Preparation of Molybdenum Disulfide Quantum Dots Using a Femtosecond Laser. *Appl. Surf. Sci.* **2020**, *511*, 145507.
(38) Sledzinska, M.; Graczykowski, B.; Placidi, M.; Reig, D. S.; El Sachat, A.; Reparaz, J. S.; Alzina, F.; Mortazavi, B.; Quey, R.; Colombo, L.; Roche, S.; Torres, C. M. S. Thermal Conductivity of MoS_2 Polycrystalline Nanomembranes. *2D Mater.* **2016**, *3*, No. 035016.
(39) Yan, Y.; Xia, B.; Ge, X.; Liu, Z.; Wang, J.-Y.; Wang, X. Ultrathin MoS_2 Nanoplates with Rich Active Sites as Highly Efficient Catalyst for Hydrogen Evolution. *ACS Appl. Mater. Interfaces* **2013**, *5*, 12794−12798.
(40) Eda, G.; Yamaguchi, H.; Voiry, D.; Fujita, T.; Chen, M.; Chhowalla, M. Photoluminescence from Chemically Exfoliated MoS_2. *Nano Lett.* **2011**, *11*, 5111−5116.
(41) Anto Jeffery, A.; Nethravathi, C.; Rajamathi, M. Two-Dimensional Nanosheets and Layered Hybrids of MoS_2 and WS_2 through Exfoliation of Ammoniated MS_2 (M = Mo,W). *J. Phys. Chem. C* **2014**, *118*, 1386−1396.
(42) Yu, Y.; Nam, G. H.; He, Q.; Wu, X. J.; Zhang, K.; Yang, Z.; Chen, J.; Ma, Q.; Zhao, M.; Liu, Z.; Ran, F. R.; Wang, X.; Li, H.; Huang, X.; Li, B.; Xiong, Q.; Zhang, Q.; Liu, Z.; Gu, L.; Du, Y.; Huang, W.; Zhang, H. High Phase-Purity 1T′-MoS_2- and 1T′-$MoSe_2$-Layered Crystals. *Nat. Chem.* **2018**, *10*, 638−643.
(43) Guo, Y.; Sun, D.; Ouyang, B.; Raja, A.; Song, J.; Heinz, T. F.; Brus, L. E. Probing the Dynamics of the Metallic-to-Semiconducting Structural Phase Transformation in MoS_2 Crystals. *Nano Lett.* **2015**, *15*, 5081−5088.
(44) Enyashin, A. N.; Yadgarov, L.; Houben, L.; Popov, I.; Weidenbach, M.; Tenne, R.; Bar-Sadan, M.; Seifert, G. New Route for Stabilization of 1T-WS_2 and MoS_2 Phases. *J. Phys. Chem. C* **2011**, *115*, 24586−24591.
(45) Alsén, N. Röntgenographische Untersuchung Der Kristallstrukturen von Magnetkies, Breithauptit, Pentlandit, Millerit Und Verwandten Verbindungen. *Geol. Fören. Stock. För.* **1925**, *47*, 19−72.
(46) Liu, G.; Robertson, A. W.; Li, M. M. J.; Kuo, W. C. H.; Darby, M. T.; Muhieddine, M. H.; Lin, Y.-C.; Suenaga, K.; Stamatakis, M.; Warner, J. H.; Tsang, S. C. E. MoS_2 Monolayer Catalyst Doped with Isolated Co Atoms for the Hydrodeoxygenation Reaction. *Nat. Chem.* **2017**, *9*, 810−816.
(47) Lau, T. H. M.; Lu, X.; Kulhavý, J.; Wu, S.; Lu, L.; Wu, T.-S.; Kato, R.; Foord, J. S.; Soo, Y.-L.; Suenaga, K.; Tsang, S. C. E. Transition Metal Atom Doping of the Basal Plane of MoS_2 Monolayer Nanosheets for Electrochemical Hydrogen Evolution. *Chem. Sci.* **2018**, *9*, 4769−4776.
(48) Le Bail, A. Whole Powder Pattern Decomposition Methods and Applications: A Retrospection. *Powder Diffr.* **2005**, *20*, 316−326.
(49) Kong, S.; Wu, T.; Yuan, M.; Huang, Z.; Meng, Q.-L.; Jiang, Q.; Zhuang, W.; Jiang, P.; Bao, X. Dramatically Enhanced Thermoelectric Performance of MoS_2 by Introducing MoO_2 Nanoinclusions. *J. Mater. Chem. A* **2017**, *5*, 2004−2011.
(50) Böker, T.; Severin, R.; Müller, A.; Janowitz, C.; Manzke, R.; Voß, D.; Krüger, P.; Mazur, A.; Pollmann, J. Band Structure of MoS_2, $MoSe_2$ and α-$MoTe_2$: Angle-Resolved Photoelectron Spectroscopy and Ab Initio Calculations. *Phys. Rev. B* **2001**, *64*, 235305.
(51) Rahman, I. A.; Purqon, A. First Principles Study of Molybdenum Disulfide Electronic Structure. *J. Phys. Conf. Ser.* **2017**, *877*, No. 012026.
(52) Imai, H.; Shimakawa, Y.; Kubo, Y. Large Thermoelectric Power Factor in TiS_2 Crystal with Nearly Stoichiometric Composition. *Phys. Rev. B* **2001**, *64*, 241104.
(53) Bourgès, C.; Barbier, T.; Guélou, G.; Vaqueiro, P.; Powell, A. V.; Lebedev, O. I.; Barrier, N.; Kinemuchi, Y.; Guilmeau, E. Thermoelectric Properties of TiS_2 Mechanically Alloyed Compounds. *J. Eur. Ceram. Soc.* **2016**, *36*, 1183−1189.
(54) Cutler, M.; Mott, N. F. Observation of Anderson Localization in an Electron Gas. *Phys. Rev.* **1969**, *181*, 1336−1340.
(55) Hébert, S.; Barbier, T.; Berthebaud, D.; Lebedev, O. I.; Pralong, V.; Maignan, A. Transport and Thermoelectric Coefficients of the Co_9S_8 Metal: A Comparison with the Spin Polarized CoS_2. *J. Phys. Chem. C* **2021**, *125*, 5386−5391.
(56) Liu, J.; Choi, G.-M.; Cahill, D. G. Measurement of the Anisotropic Thermal Conductivity of Molybdenum Disulfide by the Time-Resolved Magneto-Optic Kerr Effect. *J. Appl. Phys.* **2014**, *116*, 233107.
(57) Sahoo, S.; Gaur, A. P. S.; Ahmadi, M.; Guinel, M. J. F.; Katiyar, R. S. Temperature-Dependent Raman Studies and Thermal Conductivity of Few-Layer MoS_2. *J. Phys. Chem. C* **2013**, *117*, 9042−9047.
(58) Yan, R.; Simpson, J. R.; Bertolazzi, S.; Brivio, J.; Watson, M.; Wu, X.; Kis, A.; Luo, T.; Hight Walker, A. R.; Xing, H. G. Thermal Conductivity of Monolayer Molybdenum Disulfide Obtained from Temperature-Dependent Raman Spectroscopy. *ACS Nano* **2014**, *8*, 986−993.
(59) Sledzinska, M.; Quey, R.; Mortazavi, B.; Graczykowski, B.; Placidi, M.; Saleta Reig, D.; Navarro-Urrios, D.; Alzina, F.; Colombo, L.; Roche, S.; Sotomayor Torres, C. M. Record Low Thermal Conductivity of Polycrystalline MoS_2 Films: Tuning the Thermal Conductivity by Grain Orientation. *ACS Appl. Mater. Interfaces* **2017**, *9*, 37905−37911.
(60) Gertych, A. P.; Łapińska, A.; Czerniak-Łosiewicz, K.; Dużyńska, A.; Zdrojek, M.; Judek, J. Thermal Properties of Thin Films Made from MoS_2 Nanoflakes and Probed via Statistical Optothermal Raman Method. *Sci. Rep.* **2019**, *9*, 13338.
(61) Kim, J.-Y.; Choi, S. M.; Seo, W.-S.; Cho, W.-S. Thermal and Electronic Properties of Exfoliated Metal Chalcogenides. *Bull. Korean Chem. Soc.* **2010**, *31*, 3225−3227.
(62) Rodríguez-Carvajal, J. Recent Advances in Magnetic Structure Determination by Neutron Powder Diffraction. *Phys. B* **1993**, *192*, 55−69.
(63) Roisnel, T.; Rodríguez-Carvajal, J. WinPLOTR: A Windows Tool for Powder Diffraction Pattern Analysis. *Mater. Sci. Forum* **2001**, *378-381*, 118−123.

https://doi.org/10.1021/acsomega.1c04646
ACS Omega 2021, 6, 32783−32790